

Photon assisted tunneling of high order multiple Andreev reflections in epitaxial nanowire Josephson junctions

Damon J. Carrad,^{*,†,‡,§} Lukas Stampfer,^{†,§} Dāgs Olšteins,[†] Christian E. N. Petersen,[†] Sabbir A. Khan,^{†,¶} Peter Krogstrup,[†] and Thomas S. Jespersen^{*,†,‡}

[†]*Center for Quantum Devices, Niels Bohr Institute, University of Copenhagen, 2100 Copenhagen, Denmark*

[‡]*Department of Energy Conversion and Storage, Technical University of Denmark, Fysikvej, Building 310, 2800 Kgs. Lyngby*

[¶]*Danish National Metrology Institute, Kogle Alle 5, 2970 Hørsholm, Denmark*

[§]*These two authors contributed equally*

E-mail: damonc@dtu.dk; tsaje@dtu.dk

Abstract

Semiconductor/superconductor hybrids exhibit a range of phenomena that can be exploited for the study of novel physics and the development of new technologies. Understanding the origin the energy spectrum of such hybrids is therefore a crucial goal. Here, we study Josephson junctions defined by shadow epitaxy on InAsSb/Al nanowires. The devices exhibit gate-tunable supercurrents at low temperatures and multiple Andreev reflections (MARs) at finite voltage bias. Under microwave irradiation, photon assisted tunneling of MARs produces characteristic oscillating sidebands at quantized energies, which depend on MAR order, n , in agreement with a recently

suggested modification of the classical Tien-Gordon equation. The scaling of the quantized energy spacings with microwave frequency provides independent confirmation of the effective charge ne transferred by the n^{th} order tunnel process. The measurements suggest PAT as a powerful method for assigning the origin of low energy spectral features in hybrid Josephson devices.

Traditional Josephson junctions (JJ)¹ – where two superconductors are coupled through a thin tunnel barrier – constitute the most important device element in superconducting electronics and in state-of-the-art superconducting quantum information processors.² Recently, there has been an increasing interest in merging the quantum properties of superconductors with the electrostatic control of semiconductor electronics. For example, semiconductor-based JJs allow electrostatic tunability of the Josephson coupling,³ enabling gate-tunable superconducting qubits,⁴ and qubit implementations based on the Andreev bound states of few-channel JJs⁵ or topologically protected low-energy states in one-dimensional proximity-coupled semiconductor/superconductor hybrid devices.^{6,7} In all cases, the electronic states in semiconductor/superconductor hybrid materials are of fundamental importance. The spectrum can be probed using normal/superconductor spectroscopy^{8–10} or by measuring finite-bias transport in semiconductor JJs.¹¹ In the latter case, however, low energy spectral features can both be related to states of the leads or to higher order transport processes.^{12–14} Sharp spectral features are expected to appear at voltages $\pm 2\Delta/ne$ due to the sequential opening and closing of the allowed orders $n = 1, 2, \dots$ of multiple Andreev reflection (MAR) processes. The MAR energies are independent of the junction transparency and analysis of the SGS allows extraction of the superconducting gap^{11,15} and the determination of channel transmission of the junction.¹⁶ In nanoscale semiconductor JJs, charging phenomena^{17–19} and intrinsic properties of the semiconductor such as spin-orbit coupling can, however, modify the SGS and unambiguous assignment of MAR features in transport becomes problematic.^{20,21} This is increasingly important for processes of higher-orders – i.e. lower energy – where strong peaks unrelated to MAR can appear in the tunnel spectrum,²² heating effects may modify

the gap and thus the MAR positions, and MAR orders have been observed to be missing from the spectrum for reasons yet not understood.²³ Furthermore, understanding of the sub-gap spectrum is crucial for interpreting results from the powerful tool of superconducting scanning tunneling microscopy²⁴

A characteristic feature which could distinguish MAR processes and their orders is the transferred charge: The n^{th} -order process, dominating at $V_{sd} = 2\Delta/ne$, transfers a charge $q_n = ne$ across the junction.²⁵ While the SGS has been extensively investigated,^{12–14} only a few studies have directly addressed q_n . In Refs.^{26–28} q_n was investigated through the bias scaling of the noise spectrum of JJ which was found to be consistent with the prediction. Recently, an alternative method for measuring q_n has been suggested based on the evolution of the SGS under microwave irradiation.^{24,29,30} Due to the Tien-Gordon effect^{31,32} – or photon assisted tunneling (PAT) – modulating sidebands are expected in the non-linear SGS around the n^{th} MAR structure. While the conventional Tien-Gordon model predicts a characteristic modulation scale of $\delta V = \hbar f/e$ where f is the frequency of the microwave field, Ref.^{29,30} suggested that in higher order processes the total transferred charge should be used. This was consistent with measurement of quasi-particle tunneling ($1e$) and incoherent Cooper pair tunneling ($2e$). In this letter we present measurements of PAT of the sub-gap spectrum in epitaxial semiconductor/superconductor InAsSb/Al nanowire JJs realized by shadow lithography.^{33,34} The measurements show clear signatures of the charge $q_n = ne$ of the n^{th} order MAR up to $n = 3$.

InAsSb nanowires (NWs) were grown by molecular beam epitaxy following the procedure of Ref.³³ Parallel trenches were etched in a (100) InAs substrate and 90 – 120 nm diameter NWs were grown from Au catalyst particles positioned on opposing (111)B inclined side facets. As shown in Fig. 1a, the growth position of the NWs were laterally offset such that neighboring NWs defined ~ 100 nm wide shadow gaps^{35,36} in the 15 nm thick, in situ grown Al film (arrow).^{33,34,37} NWs were transferred to a doped silicon substrate capped with 100 nm SiO₂, and contacts to the Al half-shell were defined using established litho-

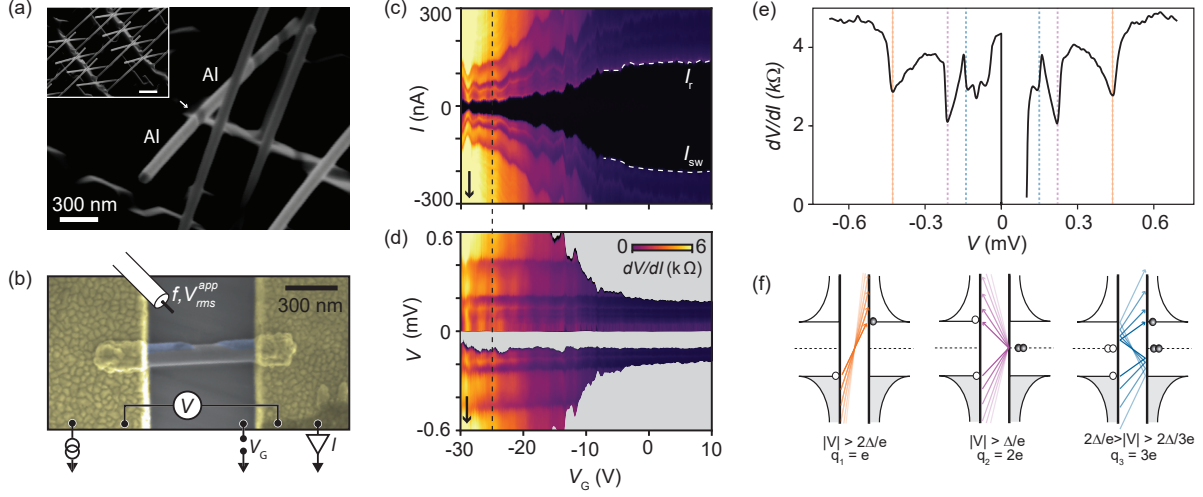


Figure 1: (a) Scanning electron micrograph (SEM) of as-grown InAsSb/Al nanowires. Al deposition was performed from roughly bottom-right to top-left across the image, and forward-positioned nanowires shadow those behind resulting in Al gaps (arrow). Scale bar in inset is 1 μm . (b) False colour SEM of a device featuring InAsSb nanowire (grey), shadow-patterned Al layer (blue) and Ti/Au ohmic contacts (gold). (c,d) Gate dependence at $T = 15$ mK of the differential resistance dV/dI vs. measured current I , and voltage V , respectively. A zero resistance supercurrent is present between switching and retrapping currents I_{sw} , I_r . (e) Line trace in (d) at fixed $V_G = -25$ V. Dashed lines indicate features at voltages $\pm 2\Delta/e$ (orange), $\pm \Delta/e$ (purple), and $\pm 2\Delta/3e$ (blue) with $\delta = 225 \mu\text{eV}$ attributed to $n = 1, 2, 3$ MAR. The corresponding transport processes are schematically illustrated in (f).

graphic methods.^{33,34,37,38} Figure 1b shows a SEM micrograph of a typical finished device and schematic measurement circuit. The conducting Si substrate acted as back-gate, which was used to alter the carrier density in the exposed InAsSb. Each contact electrode was split into two individual bond pads to facilitate pseudo-four terminal measurements of the device resistance, eliminating series resistances from e.g. low pass filters in the cryostat cabling. The remaining series resistance - likely dominated by the contacts - ~ 5 k Ω , was identified as a constant off-set in the supercurrent regime and was subtracted in the following. Measurements were performed in a dilution refrigerator with a base temperature of 15 mK and microwave radiation was coupled to the device by a coaxial line with ~ 12 mm of the inner conductor left exposed and situated ~ 5 mm above the sample.

Figure 1c shows the differential resistance, dV/dI , as a function of current through the device, I , and back-gate voltage V_G . A zero resistance supercurrent is observed for low

$|I|$. The current was swept from positive to negative (arrow) and the switching(re-trapping) current where the device transitions to(from) a resistive state from(to) the superconducting state is indicated. The differences in I_{sw} and I_{r} are commonly observed in nanowire JJs³ and ascribed to a consequence of Joule heating in the dissipative regime and/or underdamped dynamics of the JJ.^{39,40} Both I_{sw} and I_{r} decrease upon lowering V_{G} as expected from a JJ with constant $I_{\text{c}}R_{\text{N}} = \pi\Delta/2e$ and an n -type semiconductor which depletes with lowering V_{G} . Here I_{c} is the critical current and R_{N} is the normal-state device resistance. The aperiodic oscillations in $I_{\text{sw}}(V_{\text{G}})$ appearing in addition to the overall gate-dependence is attributed to universal conductance fluctuations in $R_{\text{N}}(V_{\text{G}})$.³ At $V_{\text{G}} \sim -25$ V the normal state resistance is $R_{\text{N}} \sim 4.5\text{k}\Omega$ and $I_{\text{sw}}R_{\text{N}} = 200 \mu\text{V}$, relatively close to the theoretical value $\pi\Delta_{\text{Al}}/(2e) = 350 \mu\text{V}$, as previously reported for similar hybrids.³³ The measured excess current (Supplementary Fig. S1) $I_{\text{ex}} \sim 50$ nA corresponds to a junction transmission of ~ 0.7 .⁴¹

For I above/below the zero-resistance region in Fig. 1c, dV/dI exhibits a rich structure which follow the trend of I_{sw} and I_{r} . To gain insight into the origin of these features, Fig. 1d shows the same data as a function of the measured voltage V . Upon sweeping I down from zero, the voltage remains $V = 0$ V until it abruptly switches at I_{sw} to a finite value. Therefore no data is obtained with V below this value, and this region is greyed-out in Fig. 1d. As expected for MAR, the structure in Fig. 1d appear at fixed voltages despite the variation in conductance with V_{G} . Figure 1e shows a line trace of dV/dI vs. V for fixed $V_{\text{G}} = -25$ V. The three most pronounced dips are highlighted by dashed lines and follow $\pm 2\Delta/e$ (orange), $\pm\Delta/e$ (purple), and $\pm 2\Delta/3e$ (blue) with $\Delta = 225 \mu\text{eV}$ consistent with prior results from 15 nm thick Al.^{33,38,42} This series is expected for MAR and the relevant processes transfer charges of $1e$, $2e$ and $3e$ and are illustrated in Fig. 1f, where the slopes of the arrows represent voltage biases. Direct quasi particle tunneling ($1e$) occurs for $|V| \geq 2\Delta/e$ and in general, for $n \geq 2$ the n^{th} order process involves $n - 1$ Andreev reflections, a charge transfer of ne , and is allowed within the window $2\Delta/n \leq eV \leq 2\Delta/(n - 2)$.⁴³ Overall, the dc transport

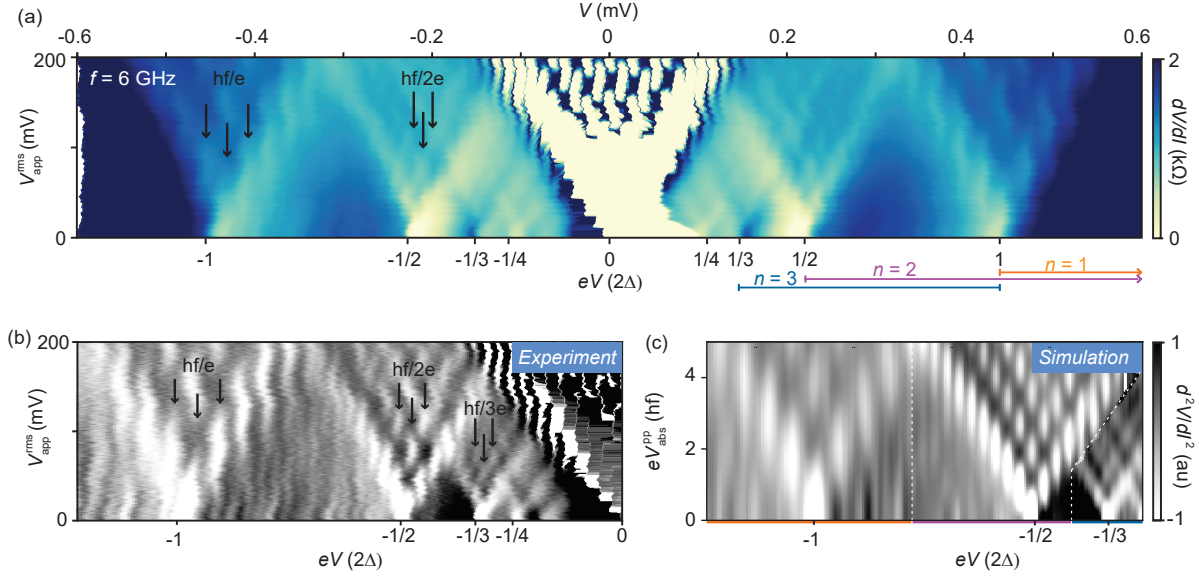


Figure 2: (a) Differential resistance at $V_G = -25V$ as a function of bias, V , and the rms amplitude of 6 GHz microwave radiation. The bottom axis represents energy E in units of 2Δ , with $\Delta = 225 \mu eV$ and the energy intervals for the first three MAR processes are indicated by horizontal lines. (b) The second derivative, d^2V/dI^2 , in a region of (a) around the higher order MAR showing the Tien-Gorden modulation in the $n = 2$ and $n = 3$ MAR processes. The changing period of modulation is indicated by arrows. (c) A simulation of the data in (b), based on Eq. 1 modified to account for the charge of the higher order transport processes. Processes of different order are assumed to dominate in the indicated regions.

characteristics in Fig. 1 are comparable to previous NW-based JJs.^{3,22,23,44}

We now consider the features arising from irradiating the device with microwaves. Figure 2a shows dV/dI vs. V and the rms amplitude, V_{app}^{rms} , of 6 GHz microwave radiation, as applied to the antenna (Fig. 1b). The gate voltage was fixed at $V_G = -25V$ as in Fig. 1e and I was swept from negative to positive. A series of ‘V’-shaped patterns are observed, fanning out from $V_{app}^{rms} = 0$. The structure emerging from $V = 0V$ – i.e., when the JJ carries a supercurrent – is due to Shapiro steps^{1,45} caused by phase-locking between the microwave field and the superconducting phase difference across the JJ leading to a step-wise increase of V in units of $hf/(2e)$. In Supplementary Fig. S2, we replot this regime as a function I as is common for studies of Shapiro steps, showing the conventional Shapiro pattern.^{3,44,46,47} The measurements are well-described by the extended RCSJ model and will not be considered further here.

The remaining V-shaped structures in Fig. 2a, which evolve from the MAR features at finite V , have a different origin and are the main focus of this work. Since the junction does not carry a supercurrent, phase locking and the resultant Shapiro steps does not occur. Instead, we attribute the structures to photon assisted tunneling. In general, for any two terminal device absorbing radiation at frequency f , charges can absorb/emit photons and thereby gain energy $\pm\hbar f$ and tunnel across the junction – here \hbar is the Planck constant and $l = 0, \pm 1, \pm 2, \dots$. Thus, at finite irradiation amplitude, the current at the dc voltage V is related to the dc current in the absence of irradiation, I^0 , at $V \pm \hbar fl/e$. For smooth $I^0(V)$, this has no consequence, however, non-linearities in $I^0(V)$ will repeat at finite radiation amplitude as sidebands with an intensity modulated by the radiation amplitude. In the simplest case where the radiation field on the sample is sinusoidal, $V_{\text{abs}} = V_{\text{abs}}^{\text{pp}} \cdot \sin(2\pi ft)$, the current at finite radiation amplitude is given by the Tien-Gordon equation:³¹

$$I_{\text{dc}}(V) = \sum_l J_l^2 \left(\frac{eV_{\text{abs}}^{\text{pp}}}{\hbar f} \right) \cdot I^0 \left(V + \frac{\hbar fl}{e} \right) \quad (1)$$

where $J_l(x)$ is the l^{th} Bessel function. The amplitude of each sideband oscillates with increasing $V_{\text{abs}}^{\text{pp}}$ according to J_l^2 (Supplementary Fig. S3). This explains the overall shape of the structures in Fig. 2a which evolve from the non-linearities at $V = 2\Delta/ne$ associated with MAR. The highly asymmetric MAR features in Fig. 1e makes the inflection points of dV/dI – i.e. peaks in d^2V/dI^2 – well suited for identifying the onset of MAR as shown in Fig. 2b. The modulation period of the features associated with the $n = 1, 2, 3$ order MARs can be clearly resolved and as highlighted by the black arrows, the modulation period is not the same for each ‘V’-fan but rather decreases with decreasing bias. This is inconsistent with the conventional Tien-Gordon model described above which predicts the same characteristic pattern evolving from all non-linearities in I^0 . Instead, as discussed in the introduction, the pattern in Fig. 2a,b follows the work of Refs^{29,30} suggesting that Eq. 1 describes the microwave response for higher-order tunnel processes if the electron charge, e , is replaced by the total transferred charge $q = ne$: Refs^{29,30} experimentally confirmed this for quasiparticle

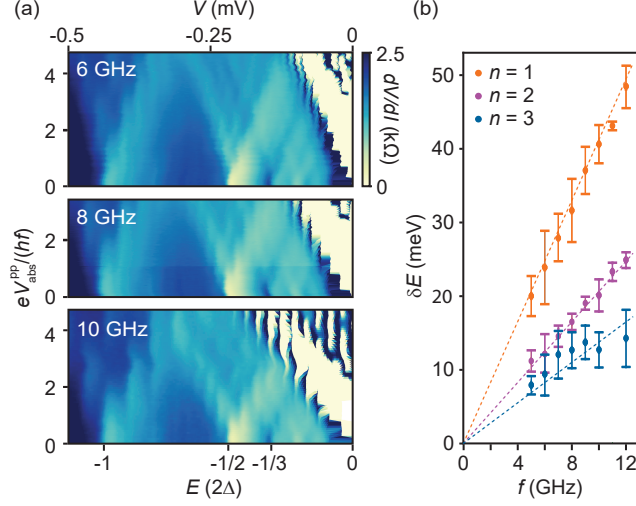


Figure 3: (a) dV/dI vs V and normalised absorbed microwave voltage $eV_{\text{abs}}^{\text{pp}}/(hf)$ for $f = 6, 8$ and 10 GHz. The 6 GHz data is a subset of Fig. 2a. The sideband spacing within each MAR order increases with increasing f . (b) Average sideband spacing $\langle \delta E \rangle$ as a function of f for $n = 1, 2, 3$ (blue, orange and green data points). The blue, orange and green dashed lines show the theoretical δE vs f relationships for 1, 2 and 3 electron processes.

(e) and incoherent Cooper pair tunneling at zero bias ($2e$). For our case, the n^{th} order MAR transfers ne electrons (Fig. 1f), and the corresponding modulation period should be $\Delta V_n = hf/ne$. For $f = 6$ GHz this amounts to $24.8 \mu\text{V}$, $12.4 \mu\text{V}$, and $8.3 \mu\text{V}$ for $n = 1, 2, 3$, respectively, in good agreement with the measured splittings $23.8 \mu\text{V}$, $12.2 \mu\text{V}$, and $9.3 \mu\text{V}$ from Fig. 2a,b (see below). Using this assumption we show in Fig. 2c the result of a simulation of d^2I/dV^2 taking the IV curve in absence of radiation as input and evolving according to Eq. 1 under the simplifying assumption that the n^{th} order MAR dominate in the region around $2\Delta/ne$ as shown by the dashed lines Fig. 2c (see Supplementary Section II for details). Comparing to Fig. 2b, the simulation accurately captures the main features of the measurement.

To further quantify the splitting, the measurements of Fig. 2a were repeated for different frequencies $f = 5 - 12$ GHz. Three representative examples are shown in Fig. 3a for $f = 6, 8, 10$ GHz. The coupling between the antenna and device depends strongly and non-monotonically on f , and therefore the amplitude of absorbed radiation, $V_{\text{abs}}^{\text{pp}}$ in Fig. 3a was for visualization purposes normalized to the first zero of J_0 which occurs at $eV_{\text{abs}}^{\text{pp}}/(hf) = 2.4$

(see Supplementary information for non-normalized data). Figure 3b shows the average of the sideband spacing $\langle \delta E \rangle = e \langle \delta V \rangle$, as a function of f (data points) and the theoretical relationship $\delta E = hf/n$ (dashed lines) for $n = 1, 2$ and 3 (blue, orange and green). The average was obtained across all the measured δE within each order, and the error bars represent the standard deviation. The good agreement between theory and experiment quantitatively confirms that the n^{th} order MAR process involves the transmission of n electrons across the junction.

In conclusion, we have studied the finite-bias sub-gap structure in epitaxial InAsSb/Al JJs under microwave radiation. We showed that the microwave response provides a sensitive probe of the transmitted charge $q = ne$ up to order $n = 3$ – i.e. a MAR process including two Andreev reflections. The modulation period was found to decrease with increasing MAR order, and the dependence of the sideband spacings on the radiation amplitude agrees quantitatively with the expectation that each order transmits n electrons across the junction. A simulation based on a modified version of the Tien-Gordon equation was found to accurately reproduce the measurements. We believe that the results will be a valuable tool for understanding the low-energy sub-gap spectrum in hybrid nanoscale devices. This becomes increasingly relevant with the rapid developments in the quality of hybrid quantum materials, device fabrication and filtering and measurement techniques, which allows for increasing coherence lengths and increased spectral resolution and thus even higher order MAR at progressively lower energies. Finally, the identification of sub-gap states is a crucial task for the powerful technique of spatially resolved superconducting scanning tunneling microscopy.

Acknowledgement This research was supported by the Danish National Research Foundation, Microsoft Quantum Materials Lab, and by research grants from Villum Fonden (00013157), The Danish Council for Independent Research (7014-00132), and European Research Council (866158).

Competing interests

The authors declare no competing interests.

References

- (1) Josephson, B. Possible new effects in superconductive tunnelling. *Phys. Lett.* **1962**, *1*, 251–253.
- (2) Kjaergaard, M.; Schwartz, M. E.; Braumüller, J.; Krantz, P.; Wang, J. I.-J.; Gustavsson, S.; Oliver, W. D. Superconducting Qubits: Current State of Play. *Annu. Rev. Condens. Matter Phys.* **2020**, *11*, 369–395.
- (3) Doh, Y.; van Dam, J.; Roest, A.; Bakkers, E.; Kouwenhoven, L.; De Franceschi, S. Tunable supercurrent through semiconductor nanowires. *Science* **2005**, *309*, 272–275.
- (4) Larsen, T. W.; Petersson, K. D.; Kuemmeth, F.; Jespersen, T. S.; Krogstrup, P.; Nygard, J.; Marcus, C. M. Semiconductor-Nanowire-Based Superconducting Qubit. *Phys. Rev. Lett.* **2015**, *115*, 127001.
- (5) Hays, M.; de Lange, G.; Serniak, K.; van Woerkom, D. J.; Bouman, D.; Krogstrup, P.; Nygard, J.; Geresdi, A.; Devoret, M. H. Direct Microwave Measurement of Andreev-Bound-State Dynamics in a Semiconductor-Nanowire Josephson Junction. *Phys. Rev. Lett.* **2018**, *121*, 047001.
- (6) Oreg, Y.; Refael, G.; von Oppen, F. Helical Liquids and Majorana Bound States in Quantum Wires. *Phys. Rev. Lett.* **2010**, *105*, 177002.
- (7) Lutchyn, R. M.; Sau, J. D.; Das Sarma, S. Majorana Fermions and a Topological Phase Transition in Semiconductor-Superconductor Heterostructures. *Phys. Rev. Lett.* **2010**, *105*, 077001.

- (8) Giaever, I. Energy Gap in Superconductors Measured by Electron Tunneling. *Phys. Rev. Lett.* **1960**, *5*, 147–148.
- (9) Deacon, R. S.; Tanaka, Y.; Oiwa, A.; Sakano, R.; Yoshida, K.; Shibata, K.; Hirakawa, K.; Tarucha, S. Tunneling Spectroscopy of Andreev Energy Levels in a Quantum Dot Coupled to a Superconductor. *Phys. Rev. Lett.* **2010**, *104*, 076805.
- (10) Pillet, J.-D.; Quay, C. H. L.; Morfin, P.; Bena, C.; Yeyati, A. L.; Joyez, P. Andreev Bound States in Supercurrent-Carrying Carbon Nanotubes Revealed. *Nature Phys* **2010**, *6*, 965–969.
- (11) Heedt, S. et al. Shadow-Wall Lithography of Ballistic Superconductor–Semiconductor Quantum Devices. *Nat. Commun.* **2021**, *12*, 4914.
- (12) Octavio, M.; Tinkham, M.; Blonder, G.; Klapwijk, T. Subharmonic energy-gap structure in superconducting constrictions. *Phys. Rev. B* **1983**, *27*, 6739–6746.
- (13) Blonder, G.; Tinkham, M.; Klapwijk, T. Transition from metallic to tunneling regimes in superconducting micro-constrictions - excess current, charge imbalance, and super-current conversion. *Phys. Rev. B* **1982**, *25*, 4515–4532.
- (14) Bratus, E.; Shumeiko, V.; Wendin, G. Theory of subharmonic gap structure in superconducting mesoscopic tunnel contacts. *Phys. Rev. Lett.* **1995**, *74*, 2110–2113.
- (15) Kjaergaard, M.; Suominen, H. J.; Nowak, M. P.; Akhmerov, A. R.; Shabani, J.; Palmstrøm, C. J.; Nichele, F.; Marcus, C. M. Transparent Semiconductor-Superconductor Interface and Induced Gap in an Epitaxial Heterostructure Josephson Junction. *Phys. Rev. Applied* **2017**, *7*, 034029.
- (16) Scheer, E.; Agrait, N.; Cuevas, J.; Yeyati, A.; Ludoph, B.; Martin-Rodero, A.; Bollinger, G.; van Ruitenbeek, J.; Urbina, C. The signature of chemical valence in the electrical conduction through a single-atom contact. *Nature* **1998**, *394*, 154–157.

- (17) Buitelaar, M.; Belzig, W.; Nussbaumer, T.; Babic, B.; Bruder, C.; Schönenberger, C. Multiple Andreev reflections in a carbon nanotube quantum dot. *Phys. Rev. Lett.* **2003**, *91*, 057005.
- (18) Eichler, A.; Weiss, M.; Oberholzer, S.; Schönenberger, C.; Levy Yeyati, A.; Cuevas, J. C.; Martin-Rodero, A. Even-odd effect in Andreev transport through a carbon nanotube quantum dot. *Phys. Rev. Lett.* **2007**, *99*, 126602.
- (19) Sand-Jespersen, T.; Paaske, J.; Andersen, B. M.; Grove-Rasmussen, K.; Jorgensen, H. I.; Aagesen, M.; Sorensen, C. B.; Lindelof, P. E.; Flensberg, K.; Nygard, J. Kondo-enhanced Andreev tunneling in InAs nanowire quantum dots. *Phys. Rev. Lett.* **2007**, *99*, 126603.
- (20) Dolcini, F.; Dell’Anna, L. Multiple Andreev Reflections in a Quantum Dot Coupled to Superconducting Leads: Effect of Spin-Orbit Coupling. *Phys. Rev. B* **2008**, *78*, 024518.
- (21) Hajer, J.; Kessel, M.; Brüne, C.; Stehno, M. P.; Buhmann, H.; Molenkamp, L. W. Proximity-Induced Superconductivity in CdTe–HgTe Core–Shell Nanowires. *Nano Lett.* **2019**, *19*, 4078–4082.
- (22) Abay, S.; Persson, D.; Nilsson, H.; Wu, F.; Xu, H. Q.; Fogelström, M.; Shumeiko, V.; Delsing, P. Charge transport in InAs nanowire Josephson junctions. *Phys. Rev. B* **2014**, *89*, 214508.
- (23) Xiang, J.; Vidan, A.; Tinkham, M.; Westervelt, R. M.; Lieber, C. M. Ge/Si nanowire mesoscopic Josephson junctions. *Nat. Nanotechnol.* **2006**, *1*, 208–213.
- (24) Peters, O.; Bogdanoff, N.; Acero González, S.; Melischek, L.; Simon, J. R.; Reecht, G.; Winkelmann, C. B.; von Oppen, F.; Franke, K. J. Resonant Andreev Reflections Probed by Photon-Assisted Tunnelling at the Atomic Scale. *Nat. Phys.* **2020**, *16*, 1222–1226.

- (25) Cuevas, J.; Martin-Rodero, A.; Yeyati, A. Shot noise and coherent multiple charge transfer in superconducting quantum point contacts. *Phys. Rev. Lett.* **1999**, *82*, 4086–4089.
- (26) Cron, R.; Goffman, M.; Esteve, D.; Urbina, C. Multiple-charge-quanta shot noise in superconducting atomic contacts. *Phys. Rev. Lett.* **2001**, *86*, 4104–4107.
- (27) Kozhevnikov, A.; Schoelkopf, R.; Prober, D. Observation of photon-assisted noise in a diffusive normal metal-superconductor junction. *Phys. Rev. Lett.* **2000**, *84*, 3398–3401.
- (28) Ronen, Y.; Cohen, Y.; Kang, J.-H.; Haim, A.; Rieder, M.-T.; Heiblum, M.; Mahalu, D.; Shtrikman, H. Charge of a quasiparticle in a superconductor. *P. Natl. Acad. Sci.* **2016**, *113*, 1743–1748.
- (29) Kot, P.; Drost, R.; Uhl, M.; Ankerhold, J.; Cuevas, J. C.; Ast, C. R. Microwave-Assisted Tunneling and Interference Effects in Superconducting Junctions under Fast Driving Signals. *Phys. Rev. B* **2020**, *101*, 134507.
- (30) Roychowdhury, A.; Dreyer, M.; Anderson, J. R.; Lobb, C. J.; Wellstood, F. C. Microwave Photon-Assisted Incoherent Cooper-Pair Tunneling in a Josephson STM. *Phys. Rev. Applied* **2015**, *4*, 034011.
- (31) Tien, P.; Gordon, J. Multiphoton process observed in interaction of microwave fields with tunneling between superconductor films. *Phys. Rev.* **1963**, *129*, 647.
- (32) Platero, G.; Aguado, R. Photon-assisted transport in semiconductor nanostructures. *Phys. Rep.* **2004**, *395*, 1–157.
- (33) Khan, S. A. et al. Highly Transparent Gatable Superconducting Shadow Junctions. *ACS Nano* **2020**, *14*, 14605–14615.
- (34) Carrad, D. J.; Bjergfelt, M.; Kanne, T.; Aagesen, M.; Krizek, F.; Fiordaliso, E. M.;

- Johnson, E.; Nygard, J.; Jespersen, T. S. Shadow Epitaxy for In Situ Growth of Generic Semiconductor/Superconductor Hybrids. *Adv. Mater.* **32**, 1908411.
- (35) Gazibegovic, S. et al. Epitaxy of advanced nanowire quantum devices. *Nature* **2017**, *548*, 434.
- (36) Krizek, F.; Kanne, T.; Razmadze, D.; Johnson, E.; Nygard, J.; Marcus, C. M.; Krogstrup, P. Growth of InAs Wurtzite Nanocrosses from Hexagonal and Cubic Basis. *Nano Lett.* **2017**, *17*, 6090–6096.
- (37) Krogstrup, P.; Ziino, N. L. B.; Chang, W.; Albrecht, S. M.; Madsen, M. H.; Johnson, E.; Nygard, J.; Marcus, C. M.; Jespersen, T. S. Epitaxy of semiconductor-superconductor nanowires. *Nat. Mater.* **2015**, *14*, 400–406.
- (38) Chang, W.; Albrecht, S. M.; Jespersen, T. S.; Kuemmeth, F.; Krogstrup, P.; Nygard, J.; Marcus, C. M. Hard gap in epitaxial semiconductor–superconductor nanowires. *Nat. Nanotechnol.* **2015**, *10*, 232–236.
- (39) McCumber, D. E. Effect of ac Impedance on dc Voltage-Current Characteristics of Superconductor Weak-Link Junctions. *Journal of Applied Physics* **1968**, *39*, 3113–3118.
- (40) Tinkham, M.; Free, J. U.; Lau, C. N.; Markovic, N. Hysteretic I-V curves of superconducting nanowires. *Phys. Rev. B* **2003**, *68*, 134515.
- (41) Flensberg, K.; Hansen, J. B.; Octavio, M. Subharmonic energy-gap structure in superconducting weak links. *Phys. Rev. B* **1988**, *38*, 8707–8711.
- (42) Deng, M. T.; Vaitiekenas, S.; Hansen, E. B.; Danon, J.; Leijnse, M.; Flensberg, K.; Nygard, J.; Krogstrup, P.; Marcus, C. M. Majorana bound state in a coupled quantum-dot hybrid-nanowire system. *Science* **2016**, *354*, 1557–1562.

- (43) Klapwijk, T.; Blonder, G.; Tinkham, M. Explanation of subharmonic energy gap structure in superconducting contacts. *Physica B+C* **1982**, *109-110*, 1657–1664, 16th International Conference on Low Temperature Physics, Part 3.
- (44) Ridderbos, J.; Brauns, M.; Li, A.; Bakkers, E. P. A. M.; Brinkman, A.; van der Wiel, W. G.; Zwanenburg, F. A. Multiple Andreev reflections and Shapiro steps in a Ge-Si nanowire Josephson junction. *Phys. Rev. Materials* **2019**, *3*, 084803.
- (45) Shapiro, S. Josephson Currents in Superconducting Tunneling: The Effect of Microwaves and Other Observations. *Phys. Rev. Lett.* **1963**, *11*, 80–82.
- (46) Larson, T. F. Q.; Zhao, L.; Arnault, E. G.; Wei, M.-T.; Seredinski, A.; Li, H.; Watanabe, K.; Taniguchi, T.; Amet, F.; Finkelstein, G. Zero Crossing Steps and Anomalous Shapiro Maps in Graphene Josephson Junctions. *Nano Letters* **2020**, *20*, 6998–7003.
- (47) Perla, P.; Fonseka, H. A.; Zellekens, P.; Deacon, R.; Han, Y.; Kölzer, J.; Mörstedt, T.; Bennemann, B.; Espiari, A.; Ishibashi, K.; Grützmacher, D.; Sanchez, A. M.; Lepsa, M. I.; Schäpers, T. Fully *in Situ* Nb/InAs-nanowire Josephson Junctions by Selective-Area Growth and Shadow Evaporation. *Nanoscale Adv.* **2021**, *3*, 1413–1421.

Supplementary Information

Supplementary Section I: Excess current

Fig. S1 shows a line trace (blue) of dc current I vs measured dc voltage V at fixed gate voltage $V_g = -25$ V extracted from the same data set used in Figure 1 of the main text. The red dotted lines show a linear extrapolation from $V > 2\Delta/e$ and the non-zero intercept corresponds to an excess current⁴¹ of $I_{\text{ex}} \sim 50$ nA corresponding to a junction transmission of ~ 0.7 .

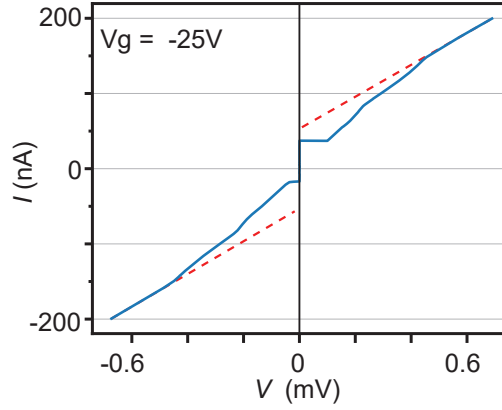


Figure S1: Measured voltage V as a function of dc current I (blue line) used to extract the excess current at fixed gate voltage $V_G = -25$ V. Red dotted lines show the extrapolation to $V = 0$ from the data for $V > 2\Delta/e$.

Supplementary Section II: Shapiro steps

Figure S2 shows the measurements of the differential resistance from main text Fig. 2a as a function of the current and the amplitude, $V_{\text{app}}^{\text{rms}}$, of the applied microwaves at 6 GHz. For $V_{\text{app}}^{\text{rms}} = 0$ mV the supercurrent appears with an asymmetry between I_r and I_{sw} as discussed in Fig. 1 of the main manuscript (the sweep direction here was from negative to positive). The asymmetry of the Shapiro steps at low $V_{\text{app}}^{\text{rms}}$ follows the I_{sw}, I_r hysteresis and has been attributed to the availability of multiple steady states at each given I for low f .⁴⁶ The pattern reproduces previous measurements of Shapiro steps in nanowire JJ.^{3,44,47} The corresponding

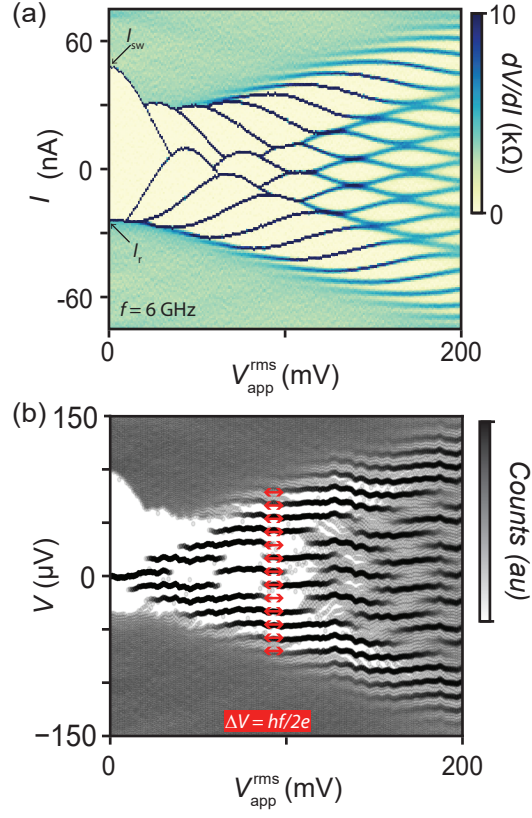


Figure S2: (a) The differential resistance as a function of the current through the InSb/Al shadow JJ and amplitude of the applied microwaves at 6 GHz. (b) A 2D representation of a histogram of the measured voltages at each V_{app}^{rms} enhancing the discrete increase of voltage in plateau in (a). Red arrow indicate steps of $hf/2e = 12.4\mu V$ corresponding to $f = 6$ GHz.

quantization of the dc voltage on the Shapiro steps is highlighted in Fig. 2c, where the grey scale represents a histogram of measured voltages; dark (light) points indicate a high (low) count of each V . The plateau values agrees with the expected value $hf/2e = 12.4 \mu\text{eV}$ as shown by the red arrows.

Supplementary Section III: PAT simulation

At finite radiation absorbed by the device, V_{abs}^{pp} , the current I_{dc} at the DC voltage V is related to the current I^0 in the absence of radiation, but evaluated at DC voltages $V \pm hf l/q$ with amplitudes given by $J_l^2(qV_{abs}^{pp}/hf)$, where $J_l(x)$ is the l^{th} Bessel function and q is the transferred charge. These amplitudes are shown in Fig. S3.

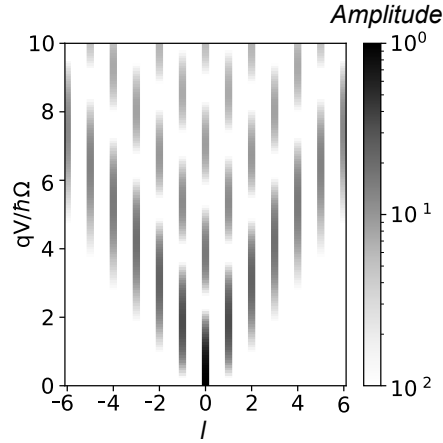


Figure S3: Plot of the Tien-Gordon amplitudes $J_l^2(qV_{abs}^{pp}/hf)$ as a function of l and qV_{abs}^{pp}/hf .

A complete description in the case of single charge transfer ($q = e$) is given by the Tien-Gordon equation

$$I_{dc}(V) = \sum_l J_l^2\left(\frac{eV_{abs}^{pp}}{hf}\right) \cdot I^0\left(V + \frac{hf l}{e}\right) \quad (2)$$

as discussed in the main text. However, in the case of PAT of MAR, up to three MAR channels may be open for a given V (see Figs 1d,2a), with the total current at $V_{abs} = 0$ the sum of the currents due to each channel, $I_{dc}^0(V) = \sum_{n \in \text{MAR}} I_n^0(V)$. For arbitrary V_{abs} ,

$$I_{\text{dc}}(V) = \sum_{n \in \text{MAR}} \sum_l J_l^2 \left(\frac{neV_{\text{abs}}^{\text{pp}}}{hf} \right) \cdot I_n^0 \left(V + \frac{hfl}{ne} \right) \quad (3)$$

with the sum over n evaluated for the allowed MAR processes at the particular V . An exact solution of equation 2 requires knowledge of each I_n^0 , which cannot be trivially extracted from the transport data in Fig. 2. However, around $V = 2\Delta/(nq)$, it is intuitive that the signal should be dominated by the n^{th} process since the other processes are at the limits of their allowed energy windows. This assumption – i.e., $I_m^0 \ll I_n^0$ for $m \neq n$ – was used to perform the calculation presented in Fig. 2c of the main text. Within each of the regions demarcated by the dotted lines and designated by the solid coloured lines below, a fixed $n = 1, 2$ or 3 was used (orange, purple, blue, respectively). In this case, the finite radiation expression reverts back to the classical Tien-Gordon equation within each region, with e replaced by ne . The good agreement between the measurement and simulation supports the attribution of the observed structure to PAT of a particular MAR order.

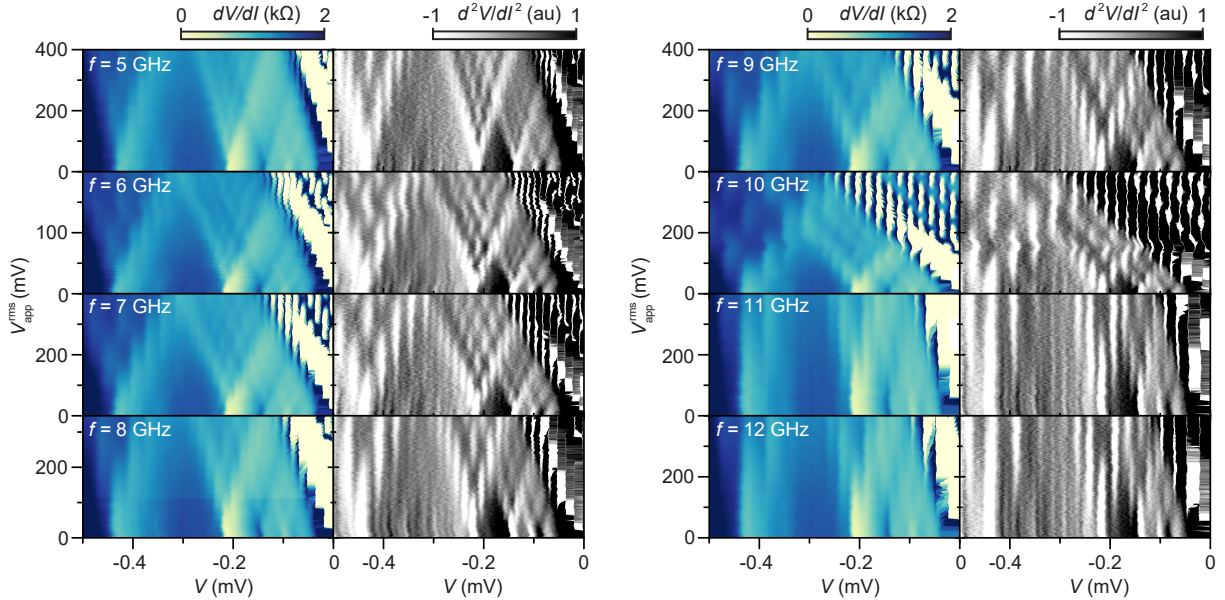


Figure S4: Differential resistance, dV/dI , (left columns) and the derivative d^2V/dI^2 (right columns) as a function of bias voltage V and applied microwave radiation amplitude $V_{\text{app}}^{\text{rms}}$ for all radiation frequencies f studied in this work. The d^2V/dI^2 data was used to analyse the side-band spacing, as presented in Fig. 3 of the main text.

Supplementary Section IV: Figure 3 underlying data

Supplementary Figure S4 shows measured dV/dI (left columns) and the numerical derivative d^2V/dI^2 (right columns) vs bias voltage V and applied microwave rms voltage $V_{\text{app}}^{\text{rms}}$ for each of the eight microwave frequencies used to extract the data in Fig. 3b of the main text. Each peak position was identified manually, with the average spacing presented as the data points in main text Fig. 3b, and the standard deviation presented as error bars. Evident in Fig. S4 is the increase in peak spacing with increasing f , as well as the non-uniform coupling between the antenna and the device. The latter causes a differing period of the oscillations in $V_{\text{app}}^{\text{rms}}$, despite the theoretical independence on f ; the period should depend solely on the properties of J_l^2 , as shown in Fig. S3. Therefore, the y-axes in Fig. 3a were scaled such that the first minima of the $n = 1, l = 0$ oscillation occurred at $eV_{\text{abs}}^{\text{pp}}/(hf) = 2.4048$, since $J_0^2(2.4048) = 0$. Using this feature allowed us to define a coupling between the device and antenna as the ratio between absorbed and applied radiation, $V_{\text{abs}}/V_{\text{app}}$. This value is plotted in Fig. S5 for the frequencies used in this paper.

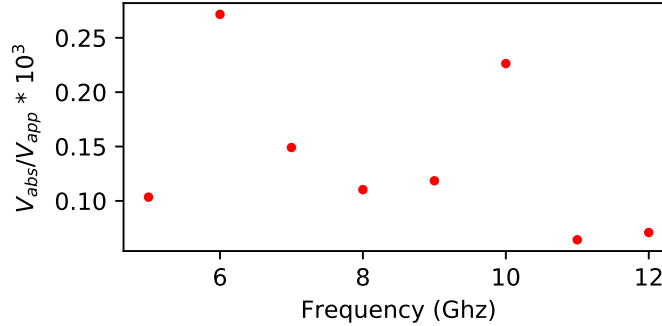


Figure S5: Frequency-dependent coupling between device and antenna, $V_{\text{abs}}/V_{\text{app}}$. The coupling was calculated from the $n = 1, l = 0$ data in Supplementary Figure S4 using the fact that the first zero of J_0^2 occurs at 2.4048. The highly varied, non-linear coupling results from the complex interaction between the microwaves and the sample environment.